Evaluating the salinity distribution of a shallow coastal aquifer by vertical multielectrode profiling (Denmark)

Søren Erbs Poulsen · Keld Rømer Rasmussen · Niels Bøie Christensen · Steen Christensen

Abstract A monitoring system, including five groups of piezometers and five vertical multielectrode profiling probes (VMEP), has been installed in an aquifer beneath a coastal dune in Denmark. In order to assess the salinity distribution within the aquifer, geoelectrical data were gathered in March, June and September 2008, by measuring a dipole-dipole and gradient array using multi-electrode profiling. Interpretation of the processed resistivity data was performed by regularized inversion using a one-dimensional, horizontally layered model of formation resistivity. The standard deviation on estimated layer log-resistivity was 0.01–0.03. By estimating two parameters of a power function, observed fluid conductivities derived from samples of porewater were related to corresponding estimated formation resistivities. The conductivity profiles correlate with a winter situation in March with high sea level, active recharge and significant wave activity, causing increased hydraulic heads, a thicker freshwater lens and salt water overlying freshwater close to the sea. In June, the thickness of the freshwater lens is reduced due to less recharge and prevailing offshore winds, imposing density-stable conditions and a sharper transition between fresh and brackish water. During the autumn, aquifer recharge is enhanced and hydraulic heads increase, resulting in a thicker freshwater lens.

Keywords Coastal aquifers · Geophysical methods · Multielectrode profiling · Salinity distribution · Denmark

Received: 19 December 2008 / Accepted: 29 June 2009
Published online: 8 August 2009

S. Erbs Poulsen (✉) · K. Rømer Rasmussen · N. Bøie Christensen · S. Christensen
Department of Earth Sciences,
University of Aarhus,
Høegh-Guldbergs Gade 2, bld. 1670, 8000, Aarhus, Denmark
e-mail: soeren.erbs@geo.au.dk
Tel.: +45-8942-5524

K. Rømer Rasmussen
e-mail: geolkrr@geo.au.dk

N. Bøie Christensen
e-mail: nbc@geo.au.dk

S. Christensen
e-mail: sc@geo.au.dk

Introduction

Coastal aquifers are complex flow systems driven by processes varying on several timescales. Seasonal variations in recharge may introduce delayed oscillations in the submarine groundwater discharge (SGD) due to the percolation time of precipitation through the unsaturated zone (Michael et al. 2005). Tidal oscillations and wave activity, acting on a sloping beach, lift the aquifer water table and subsequent aquifer waves are damped and lagged as they travel inland (Nielsen 1990; Nielsen et al. 1997; Cartwright et al. 2003; Li et al. 1999a). A seepage face may develop as the ocean water retracts during ebb tide or storm events, further complicating the boundary condition at the coastline as studied both analytically (e.g. Li et al. 1999b; Turner 1993) and numerically by Li et al. (1997). The dynamic nature of groundwater flow in coastal aquifers thus incurs large variations in porewater salinity in space and time.

Different quantitative methods can be adopted for investigating groundwater flow and solute transport in coastal aquifers. Geochemical tracers and water sampling studies are reported by e.g. (Povinec et al. 2006; Charette et al. 2003; Swarzenski et al. 2007; Young et al. 2008; Burnett et al. 2008; Moore 2007; Moore and de Oliveira 2008). Numerical flow modelling studies have been carried out by e.g. (Vandenbohede and Lebbe 2006; Michael et al. 2005; Christensen and Engesgaard 2000; Smith and Zawadzki 2003; Mao et al. 2005). Geophysical methods including geoelectrical and electromagnetic geophysical surveys are reported by e.g. Kafri et al. (1997); Turner and Ackworth (2004) in combination with (1) gravimetry (Duque et al. 2008), (2) reflection seismics (Shtivelman 2000; Choudhury et al. 2001), (3) magnetic resonance soundings (Vouillamoz et al. 2007) and (4) numerical flow modeling (Bouzouf et al. 2001; Koukadaki et al. 2007). An overview of different approaches is given by Oberdorfer (2003).

The objective of the present study is to investigate the seasonal changes in porewater salinity of a shallow aquifer

 DOI 10.1007/s10040-009-0503-6

below a coastal dune extending ~165 m perpendicular to the coastline with a saturated thickness of ~10 m. Vertical, geoelectrical probes with evenly distributed electrodes have been installed in the aquifer. By measuring vertical profiles, resistivity data are collected, processed and interpreted using a model of formation resistivity with a vertical resolution of 0.25 m. This paper presents details of the instrumentation at the field site and demonstrates the method of vertical resistivity profiling and the processing of resistivity profiles. The interpretation of three VMEP (vertical multielectrode profiling) profiles, taken in March, June and September 2008, is carried out by regularized inversion using a layered, one-dimensional model of formation resistivity. The relation between formation resistivity and porewater salinity is obtained by using a power law model (Turner and Ackworth 2004).

Field site and instrumentation

The field site is located at the Danish North Sea coast on a coastal barrier separating a bay (Limfjorden) from the sea (Fig. 1). The barrier is transgressional and groynes have been built every 500 m along the shore in order to protect the beach against erosion. From the shore, the beach rises to about 2.5 m approximately 60 m inland where wave erosion during storm events has formed a 1–2-m-high escarpment. Further to the east, a 100-m-wide ridge of 4–5-m-high sparsely vegetated coastal dune separates the beach from a flat 1-km-wide inland lagoon featuring lakes and vegetated areas which delineate the barrier towards the bay (Fig. 2). During the Pleistocene, a thick clay deposit was formed in the bay which at that time reached further to the west. Today, the top of this deposit is located at about −9 m at the field site (all elevations are relative to datum which is mean sea level, [masl]). Samples from five boreholes (E1–E5, Fig. 2) drilled between the lagoon and the beach show that generally the sequence between the top of the clay and the surface coarsens upwards. Thus, the clay is first overlain by ~8 m of silty fine sand while above, fine to medium sand is found. However, to the east (E1–E3), a 10–25 cm layer of clayey silt is found at about −1 m, apparently separating the silty fine sand from the fine-medium sand. Annual precipitation at the coast is about 800 mm, while potential evapotranspiration is about 500 mm. Actual evapotranspiration is somewhat smaller (maybe only half that value) on the beach and the dune because of the sparse vegetation. In autumn and winter, when precipitation is high and evapotranspiration low, the excess rain water percolates through the vadose zone. In the lagoon, where the water table is never much below the surface, excess water may result in partial or total flooding. The coastal dune forms a shallow coastal aquifer where recharging water percolates through the vadose zone. Because the vadose zone on average is several meters thick there will be a lag from when water infiltrates in the top of the dune to when recharge of the aquifer takes place. A dike surrounds the lagoon towards the bay, but during fall and winter storms, when the sea level in the North Sea and the bay rises, water will flow into the lakes in the lagoon through a small channel. During spring and summer, the connection to the bay is closed during high sea level by a sluice which prevents flooding.

In the fall of 2007, a set of VMEP probes were installed in five cased boreholes, E1–E5. In E1–E4, the bottom electrode was placed at −5 m, while at E5 it was placed at −3.7 m. Having placed the probes, the casing was removed allowing the sediments to collapse around the probes. The VMEP probes are constructed from a 60-mm quadratic-glass fibre tube with 6 mm wall thickness. Electrodes, made of 10-mm stainless SAE (Society of Automotive Engineers) grade 316 steel (Bringas 2004), are placed around the glass fibre tube every 0.25 m, and connected through a sealed connection to the cabling inside the tubes running to the upper end of the probe. To give additional protection, the probe was filled with epoxy

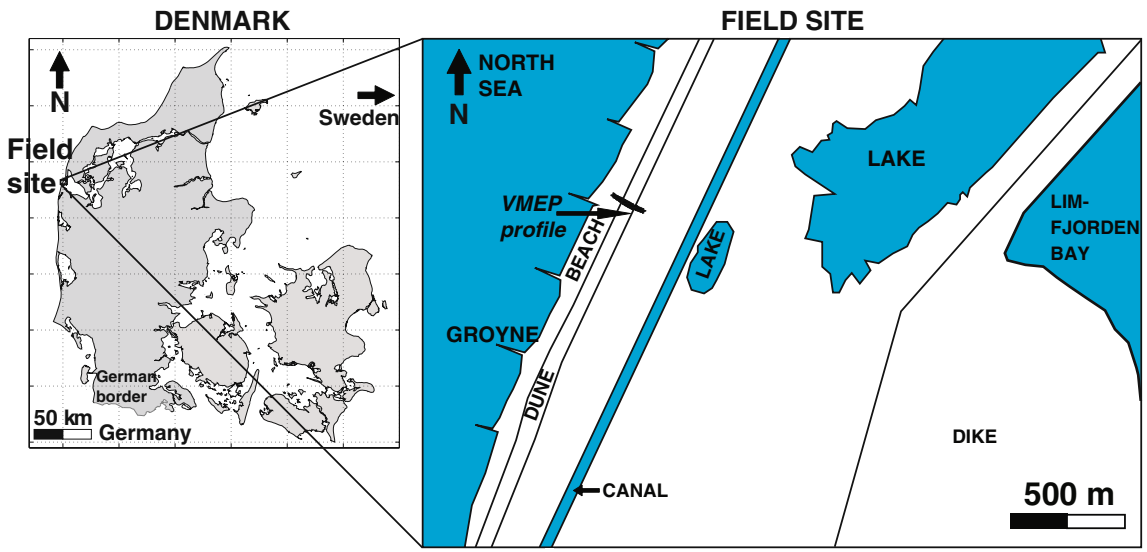

Fig. 1 The field site including the vertical multielectrode profiling (VMEP) profile at the Harboøre Barrier, Denmark

 DOI 10.1007/s10040-009-0503-6

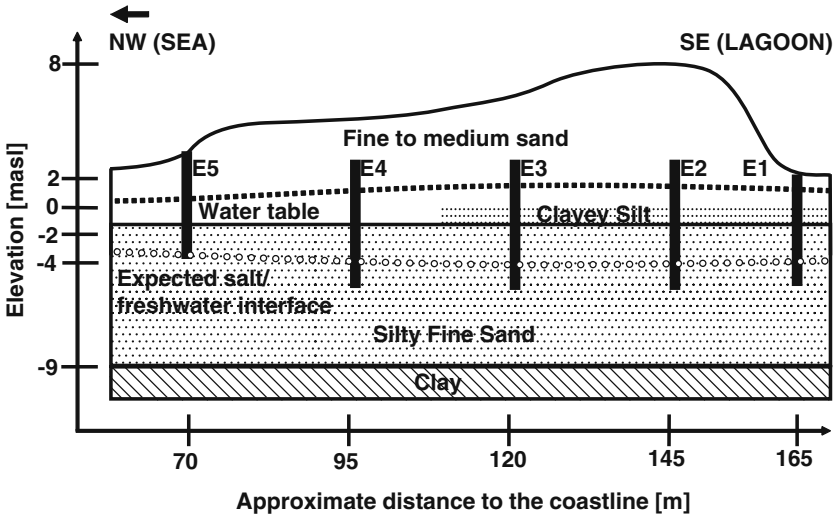

Fig. 2 Geology and instrumentation along the VMEP profile. *Dashed line*: water table; *dot/circle line*: freshwater/salt-water interface; probes are shown as *elongated black rectangles* (E1–E5)

after connecting the wiring at the end to a cable terminating in a box at the surface. Due to the different lengths of the probes, the number of electrodes varies: at E1 and E5 there are 28 electrodes while at E2–E4 there are 32 electrodes. Approximately 1 m from each VMEP probe, three 63-mm piezometers were installed with the screen top at approximately 0, −2 and −4.5 m as illustrated in Fig. 3. Each screen is 0.5 m long. Slug tests made in some of the piezometers during 2007 indicated that the hydraulic conductivity of the silty fine sand is about $1.0 \bullet 10^{-6}$ m/s while that of the fine to medium sand is $5.0 \bullet 10^{-5}$ m/s.

The tidal amplitude is ~0.25 m at the field site. Tidal oscillations shift the coastline ~5 m horizontally. In the lagoon, the response from tidal oscillations is expected to be significantly damped and lagged. During episodic storm surges the sea level rises up to 2.5 m. The average distance from E5 to the coastline is ~70 m. Episodic storm surges can reduce the distance between the coastline and E5 to less than 10 m and wave run-up may reach the probe during such events. None of the VMEP probes were inundated by seawater during the profiling in March, June and September 2008.

Method

Collecting geoelectrical data by means of electrode profiling requires a complete protocol containing the configuration of potential and current electrodes for each measurement. Apparent resistivity ρ_a [ohm metres, Ωm] is defined as the measured difference in potential ΔV [V] normalized by the current I [A] and multiplied by a geometric factor K [m] in the following equation:

$$\rho_a = K \frac{\Delta V}{I} \quad (1)$$

where K depends on the type of array. Quality control of the resistivity data is done through a visual inspection of data pseudo-sections and profile plots so that outliers can be identified and culled from the data set. Estimates of formation resistivity are obtained by regularized inversion of the resistivity data based on a one-dimensional, multi-layered earth model. The salinity distribution is estimated by establishing a relationship between porewater conductivity and formation resistivity.

Vertical multi electrode profiling

The choice of electrode configuration is based on the requirement for vertical resolution. Measurements are

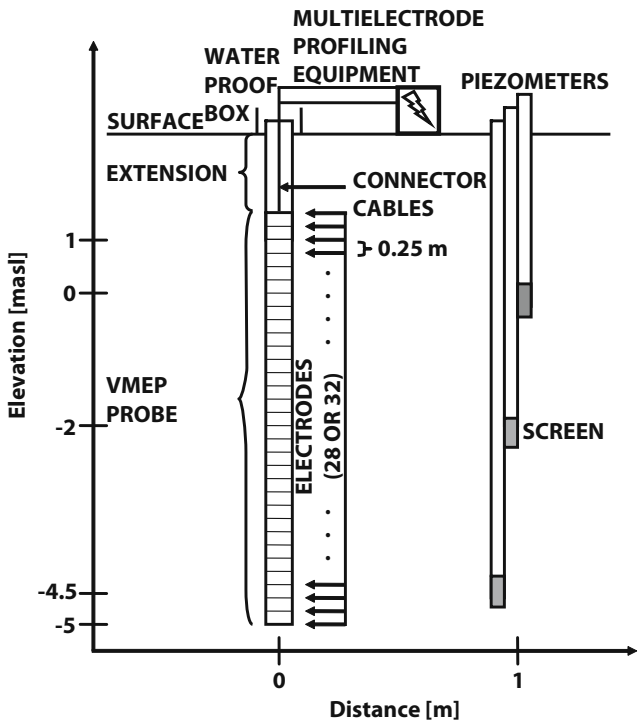

Fig. 3 A VMEP probe accompanied by three piezometers screened at different depths

 DOI 10.1007/s10040-009-0503-6

carried out in two configurations. One is the gradient configuration where all potential dipoles of unit length are measured between two current electrodes. The current electrode distances are chosen as 9, 18, 21, 24, 25 and 27 unit lengths for the short probe and 9, 18, 24, 27, 28 and 30 unit lengths for the long probe with overlapping sections. The second configuration is the dipole-dipole configuration where current and potential dipole lengths from one unit distance to 7 unit distances are used. The dipole-dipole configuration is good at defining layer boundaries, but the signal-to-noise ratio is not always the best. The gradient configuration has been shown to be sub-optimal in most cases (Dahlin and Zhou 2004) and provides a good signal-to-noise ratio for all measurements. When an electrode has been used as a current electrode, it will carry a potential for some time afterwards. During this period, serious measurement noise will be the result of using the electrode in a potential measurement. Therefore, the measurement protocols are designed to maximize the time between using an electrode as a current and a potential electrode while keeping the overall runtime of the protocol to a minimum. The runtime is ~20 min for each protocol yielding one set of profiling data in ~40 minutes. Standard MEP (multielectrode profiling) equipment, consisting of a Terraohm RIP924 electrical resistivity meter, SAS2000 booster and an ES10-64 electrode selector, is connected to the probe and data is gathered by a field laptop using the ABEM software ERIC v2.09 from www.abem.se. The profiles in March were measured using a different SAS2000 booster, as the original booster malfunctioned during the field measurements. For all measurements, the signal-to-noise ratio is good and reciprocal measurements were not collected. The current was set to 200 mA in all measurements.

Water sampling

500 ml of water was retrieved from each of the piezometers. A submersible pump was lowered inside the piezometer to the bottom of the screen and prepumped to remove stagnant water prior to the water sampling. The water conductivity was measured by a portable multi-parameter instrument (Pioneer 65 from Radiometer Analytical). The conductivity meter was calibrated to a 1,015 μ*S*/*cm* standard solution.

Processing

Bad data points may be caused by failure of the relays at one of the electrodes, poor electrode-sediment contact due to dry soil in the unsaturated zone, or shorting between cables due to leaking salt water. Such data are often represented by apparent resistivity values that are significantly larger or smaller compared to neighboring data points. Processing is carried out by visually inspecting apparent resistivity values plotted against their vertical position in the profile (the pseudo-section). Resistivity values differing considerably from neighboring points are removed from the dataset. In this study, the pseudo-section is calculated using the software ERIGRAPH v2.18.09 from www.abem.se. Figure 4a is an example of a pseudo-section in which an outlier can be identified in the deepest part of a profile.

Inversion of resistivity data

There are numerous approaches to the inversion of geophysical data with a one-dimensional model consisting of horizontal, homogeneous and isotropic layers. The one used for the VMEP data is a well-established iterative-damped least-squares approach (Inman et al. 1973;

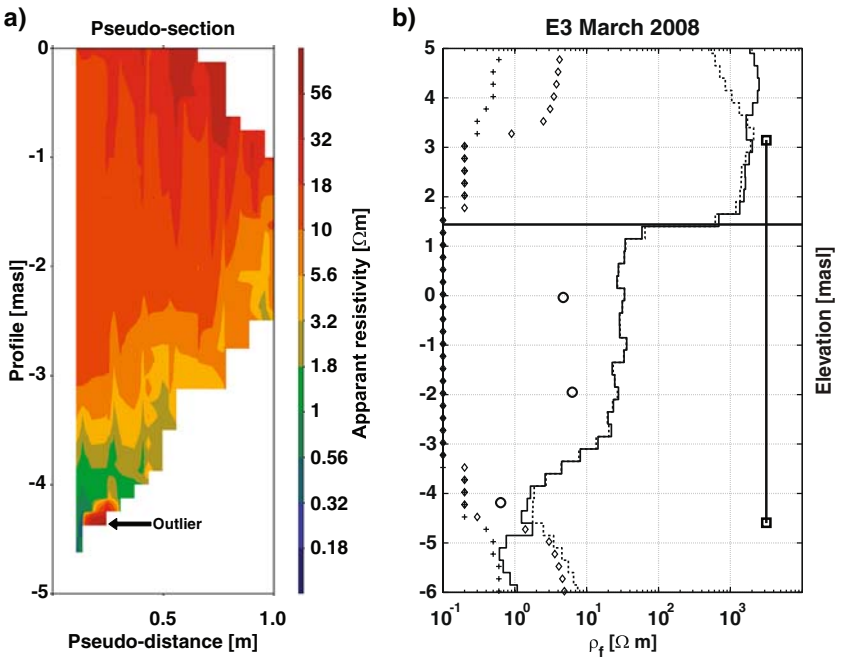

Fig. 4 **a** Pseudo-section containing an outlier; **b** example of two estimated model curves of formation resistivity ρ_f using standard deviations of the model covariance matrix σ_0=0.1 (*dashed line*) and σ_0=1 (*solid line*) and corresponding 10× SD curves for σ_0=0.1 (*line with crosses*); σ_0=1 (*line with diamonds*); water table *(thick horizontal line)*; water sample (*circle*); and the probe (*solid line with square end-markers*)

 DOI 10.1007/s10040-009-0503-6

Tarantola 1987; Menke 1989). Formally, the model update at the n'th iteration is given by

$$m_{n+1} = m_n + \left[G_n^T C_{obs}^{-1} G_n + C_m^{-1} + \lambda I\right]^{-1} \cdot \left[G_n^T C_{obs}^{-1}(d_{obs} - g(m_n)) + C_m^{-1}(m_{prior} - m_n)\right] \quad (2)$$

where m is the model vector containing the logarithm of the model parameters, G is the Jacobian matrix containing the derivatives of the data with respect to the model parameters, T is the vector transpose, C_{obs} is the data error covariance matrix, C_m is a model covariance matrix imposing the vertical smoothness constraint of the multi-layer models, λ is the Marquard damping factor, I is the identity matrix, d_{obs} is the field data vector, $g(m_n)$ is the nonlinear forward response vector of the n'th model, and m_{prior} is the prior model vector. The forward responses are modelled in the wavenumber domain through recursion formulas (Daniels 1978), and the Hankel transform from wavenumber to space domain is calculated using the filters of Christensen (1990). In this study, as is most often the case, the data noise is assumed to be uncorrelated, implying that C_{obs} is a diagonal matrix. There is also no prior information included on the model parameters. The model used for the inversion of all resistivity data is a multi-layer model, where the subsurface is divided into 60 layers, 59 of which are 0.25 m thick and the bottom layer stretches to infinity. Thus, independent of the depth of installation of the vertical probes, the model discretizes the top 15 m of the subsurface, enough to cover all probe intervals. In the iterative inversion, the layer boundaries are kept fixed and only the layer resistivities are changed in the inversion. To avoid geologically unrealistic models with rapidly varying resistivities, vertical constraints are introduced through the model covariance matrix. The model covariance matrix C_m is constructed by stacking single-scale exponential covariance functions with different correlation lengths in such a way that they will approximate a von Karman covariance function. According to Serban and Jacobsen (2001) this is possible if we choose

$$\Phi_{\nu,L_n} \approx \sigma_0^2 \sum_{j=0}^{N} C^{j\nu} \exp\left(-\frac{|z|}{C^j L_n \cdot 0.65}\right) \quad (3)$$

where $\Phi_{\nu,\ Ln}$ is the von Karman covariance function of order ν and correlation length L_n, C is the factor ($C<1$) between the correlation lengths, N is the number of stacked single-scale covariance functions, σ_0 is the standard deviation of the correlation and z is the distance in space. In this study, we have used ν=0.1, C=0.1, L_n= 100,000 km and N=10. This means that the covariance function will contain correlation lengths between 0.65 cm and 6,500 km, one per decade. This covers scales of geological variability between the radius of the Earth and pebbles. Using the broadband covariance functions defined above ensures that model structure on all scales will be permitted if required by the data. Note that the model covariance matrix only depends on the geometry of the multilayer model and so needs to be calculated and inverted only once for the whole data inversion process. The broadband covariance function also has the desirable property that, for a given σ_0, the regularization level does not depend on model discretization. Inversion was carried out with an initial (prior) model with a resistivity of 10 Ωm in all layers, but with two different standard deviations of the model covariance matrix: σ_0=0.1 and σ_0=1.0. An appropriate level of regularization of the inversion was decided pragmatically by inspecting the results of using different values. In this case, there was very little difference between the results for a wide range of values because there is good data coverage in the depth interval of the electrodes. Within the permissible range, we chose a value of 0.1 which gives a tight regularization and a value of 1.0 which gives a weak regularization. Where data controls the final model, the two models will be almost similar and where data have only a weak influence, the two models will differ because the model with the tighter constraint of σ_0=0.1 is more strongly tied to the prior model. The two models can be used to evaluate inversion quality. The comparison of the two models is supported by a comparison between the relative uncertainty of the layer resistivities in the two cases. The two curves will diverge where data has little influence on the inversion result. As expected, the resistivity model can be trusted only in the depth interval covered by the electrodes. Figure 4b includes an example of two estimated model curves of formation resistivity using σ_0=0.1 and σ_0=1 respectively, in March 2008 for probe E3.

The model parameter uncertainty estimate relies on a linear approximation to the posterior covariance matrix, C_{est}, given by

$$C_{est} = \left[G^T C_{obs}^{-1} G + C_m^{-1}\right]^{-1} \quad (4)$$

where G is based on the final model. The analysis is expressed through the standard deviations (SD) of the model parameters obtained as the square root of the diagonal elements of C_{est} (e.g. Inman et al. 1973).

Relating formation resistivity to porewater conductivity

Relating formation resistivity to fluid conductivity depends on the type of sediment and the conductivity of the porewater. Archie (1942) provides a linear relation between formation and porewater resistivity, ρ_f (Ωm) and ρ_w (Ωm) respectively, which in terms of the electrical conductivities σ_w and σ_f (S/m) is

$$\sigma_w = F\sigma_f \quad (5)$$

where the proportionality constant F is the "formation factor" which is related to the porosity of the sediment.

DOI 10.1007/s10040-009-0503-6

Equation 5 is valid for sediments where the matrix resistivity is high and where the porewater is the main conductor. For clayey sediments containing freshwater with conductivities less than 0.5 S/m, the sediment itself is a significant conductor and formation resistivity becomes a non-linear function of porewater conductivity. Porewater with conductivities below 0.5 S/m is present in the upper part of the aquifer at the field site and clayey silt is encountered around −1 m (Fig. 2). Therefore formation resistivity and porewater conductivity is related by a power function as proposed by Turner and Ackworth (2004)

$$\rho_f = \frac{A}{\sigma_w^B} \tag{6}$$

The parameters A and B in Eq. 6 are estimated by linear regression of log-transformed observed porewater conductivities.

$$log(\rho_f) = log(A) - B \cdot log(\sigma_w) \tag{7}$$

Water samples are gathered from piezometers with a screen length of 0.5 m which makes it difficult to determine the exact depth for which the salinity of the water sample is representative. Therefore, the estimated formation resistivity used in the estimation of Eq. 7 is calculated as an average over the three model layers situated closest to the screen.

Results

March, June and September 2008 represent different distributions of hydraulic head and salinity which depend on both the sea level and aquifer recharge. Sea level records and estimated recharge are found in Fig. 5. Recharge was computed with a simple root-zone model (Christensen 1994) using local daily precipitation and evapotranspiration data and a 10 mm root-zone capacity.

The effect of tidal oscillations on the water table within the beach is expected to be most significant in March where the coastline is closest to probe E5 compared to that of June and September. The water table $h(x,t)$ as a function of time t and the distance from the coastline x in an unconfined, homogeneous aquifer subject to tidal oscillations, and not considering recharge is

$$h(x,t) = A\cos(\omega t - kx)e^{-kx} \tag{8}$$

where A [L] is the tidal amplitude; $k = \sqrt{\frac{n\omega}{2KD}}$ [L^{-1}] is the wavenumber in which n is the porosity; ω [rad/T] the angular frequency of the tidal oscillation; K [L/T] is the hydraulic conductivity; and D [L] the height of the mean sea level over the bottom of the aquifer (e.g. Kovac 1981). Equation 8 implies that tidal oscillations are damped exponentially as a function of the wavenumber and the distance from the coastline. Considering only the upper sandy sequence extending down to −1 m and using parameter values specific to the field site, a maximum tidal wave amplitude of less than 1 mm is expected at E5 in March, June and September which indicates that the dynamic effect of tidal oscillations on the water table is negligible at E5. The lifting of the aquifer water table due to tides is ≈5 cm as estimated by the analytical model of Nielsen (1990; p. 2132). The wave setup at the coastline is ~0.4 times the off-shore root-mean-square wave height H_{rms} (Turner et al. 1996). The offshore H_{rms} relevant to the field site, varies between 25 and 75 cm (Woolf et al. 2002) implying a wave setup of between 10 and 30 cm at

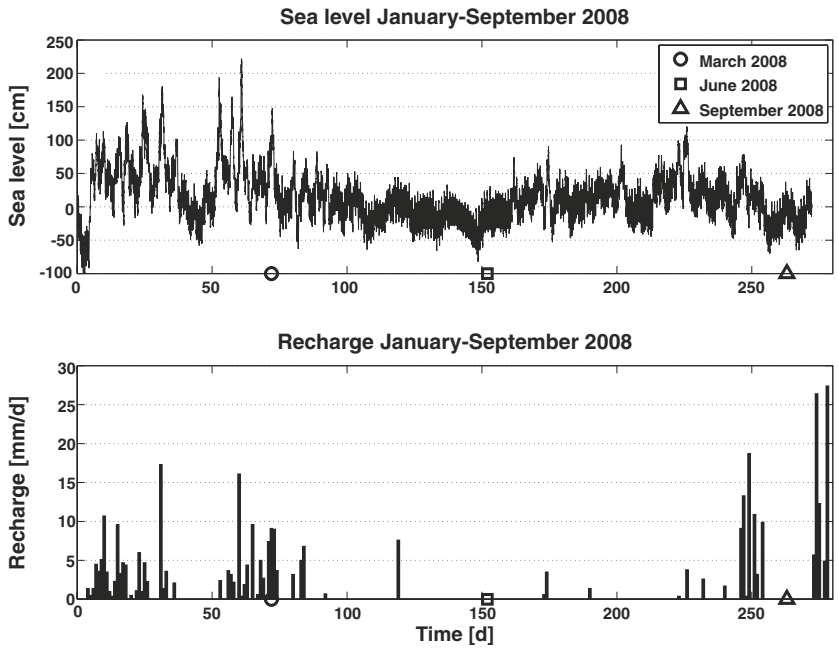

Fig. 5 Sea level (above mean sea level) and estimated daily recharge January–September 2008

 DOI 10.1007/s10040-009-0503-6

the coastline. Thus, the impact of tides on hydraulic head, at the VMEP profile is relatively small under normal climatic conditions.

In the processing of the fifteen profiles gathered in March, June and September, only 0.8% of the data were eliminated from the dataset. The standard deviation obtained from Eq. 4 on estimated log-resistivity is generally between 0.01–0.03 except at E1 in September where uncertainties increase from 0.02 to 0.20 between −3.75 and −2.25 m, which can be attributed to missing data from five electrodes at this depth (Table 1). It may be related to either a missing contact with the connecter sockets or to intruding water which, despite all efforts to encapsulate the wiring within the probe, may have breached the filler. Data residuals are largest in March and September at E1 and E5. The differing residuals may be related to the use of a different booster in March which may incur different levels of noise on the resistivity measurements. This however, does not explain why the data residuals are higher in September, as the profiling in June and September was carried out using the same equipment. Residuals can be reduced by increasing the number of model layers and/or increasing the predefined uncertainty on observed, apparent resistivity. Thus, for different distributions of salinity, a finer model discretization may be required to obtain low residuals.

Porewater conductivity

Figure 6 contains three contour profiles of the water-sample salinity in March, June and September 2008. Water samples gathered from the piezometers situated at −4.5 and −2 m have salinities of >20,000 and <2,500 ppm, respectively. It is not possible to delineate the freshwater/salt water transition zone between −4.5 and −2 m on the basis of water samples alone for any of the profiles.

The parameters A and B of Eq. 7 were estimated from observed porewater conductivity and modeled formation resistivity gathered in March, June and September (Fig. 7).

Models relating formation resistivity and porewater conductivity can also be estimated on the basis of observations from March, June and September separately (Fig. 8). For each of these models, the individual 95% prediction interval was computed (95% confidence limits for an individual observation, Draper and Smith (1981)) and then compared with the observations made at the two other times (the prediction intervals are not shown on Fig. 8 since they would make the figure almost unreadable). Because the measurements made in March are widely scattered around the regression line, the prediction interval for March is wide and contains all measurements made in June and September. Contrary to this, the data for June and the data for September are closer to each of their regression lines, and the prediction intervals for the June and September models are therefore narrower. As a consequence, data from June is found to fall systematically outside the prediction interval for the September model, and vice versa. This indicates that the model relating formation resistivity and porewater conductivity for June is significantly different from the model for September. However, as the clay content is insignificant at its maximum of 4.5% in the clayey silt, there is currently no physical explanation for the models to be different. The separate models are used for converting the resistivity profiles in June and September as they are statistically distinguishable. The resistivity profile in March is converted by using the general model based on all available observations (A and B from Fig. 7).

The estimated values of porewater conductivity based on formation resistivities with a standard deviation less than 0.03 on log-transformed parameters (except for E1 between −3.75 and −2.25 m) are found in Fig. 9.

March

Hydraulic heads are at a maximum in March compared to observed heads in June and September. The sea level was high compared to that of June and September, decreasing from 100 to 81 cm during the profiling (relative to datum which is mean sea level). The coastline was ~45 m from E5. The hydraulic gradient between E1 and E2 is directed towards the lagoon which may be attributed to aquifer discharge into lagoon surface water which provides a pathway for rapid surface-water runoff. The conductivity profile suggests a thick freshwater lens due to favorable recharge conditions throughout January–February. In March, saline water tops freshwater at E5. A freshwater zone of 0.14 to 0.27 S/m extends to −2.1 m at E1, −2.7 m at E2, and −3.0 m at E3 and E4, topping a transition zone where porewater conductivity gradually increases from 0.27 to 4.45 S/m. The thickness of this transition zone varies from 0.75 m at E1–E2, 1 m at E3 and 1.25 m at E4. At E5 porewater conductivity decreases from 3.45 to 2.32 S/m between 0.6 and −1.7 m, and from 1.21 to 0.82 S/m below −1.7 m, implying saline water topping freshwater in an unstable density distribution. The lower conductivities observed at 0.8–1.5 m at E5 may be attributed either to recent freshwater infiltration or to the presence of a 2 m long PVC pipe enclosing the upper part of the probe down to 1.5 m, installed to secure the probe from waves during storm events.

June

Very low recharge took place throughout April–May 2008 because of low precipitation which, combined with a relatively low average sea level due to prevailing offshore winds, ultimately lowered the aquifer water table in June by 0.5–1 m below that of March 2008. The sea level

Table 1 VMEP data residuals and standard deviation (SD) on log-transformed parameters

VMEP 2008	March	June	September
Data residual	1.9–4.1	1.0–2.4	1.8–3.5
Parameter SD (10^{-2})	1–2	1–2	1–3 (20)

DOI 10.1007/s10040-009-0503-6

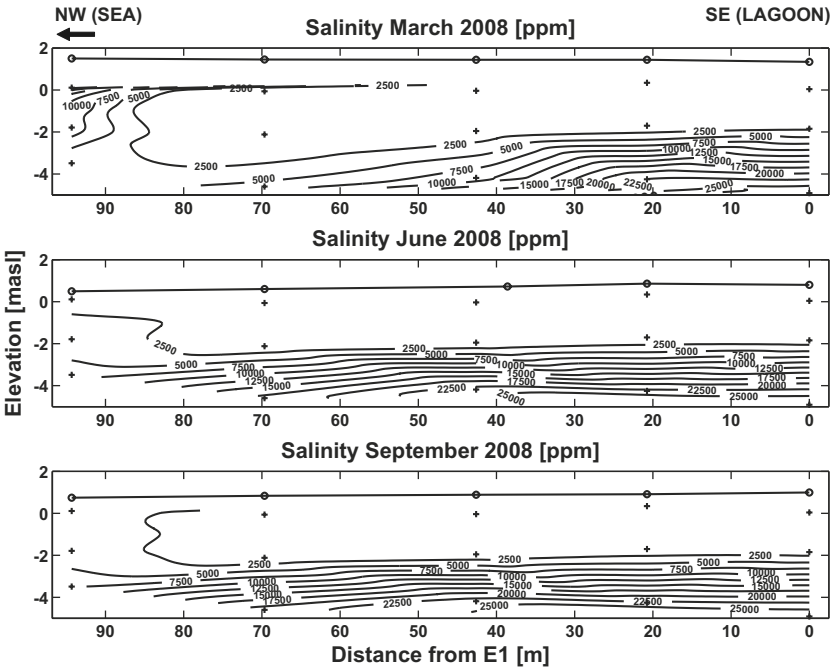

Fig. 6 Interpolation of water sample salinity March, June and September 2008; (*line with circles*) water table; (*line with crosses*) water sample point; equidistance=2,500 ppm

decreased from 9 cm to −25 cm during the profiling and the coastline was ~65 m from E5. As in March, a hydraulic gradient towards the lagoon is present between E1 and E2. In June, at E1–E4 conductivities suggest more saline conditions compared to March, except at E5 where saline water overlies fresh water in March. The freshwater zone conductivities span 0.14–0.37 S/m while the transition zone varies between 0.37–4.55 S/m. At E5, a zone of 0.29–0.71 S/m reaches −3 m where conductivities increase further to 0.71–1.39 S/m. The width of the transition zone between freshwater and brackish water varies from 0.5 m at E1–E2, 0.75 m at E3 and 1 m at E4 thus illustrating the sharpest freshwater/salt-water interface among the three profiles. The extent of the brackish zone is significantly larger compared to that of March and September.

September

The late summer of 2008 was unusually wet, providing increased recharge. Combined with prevailing on-shore

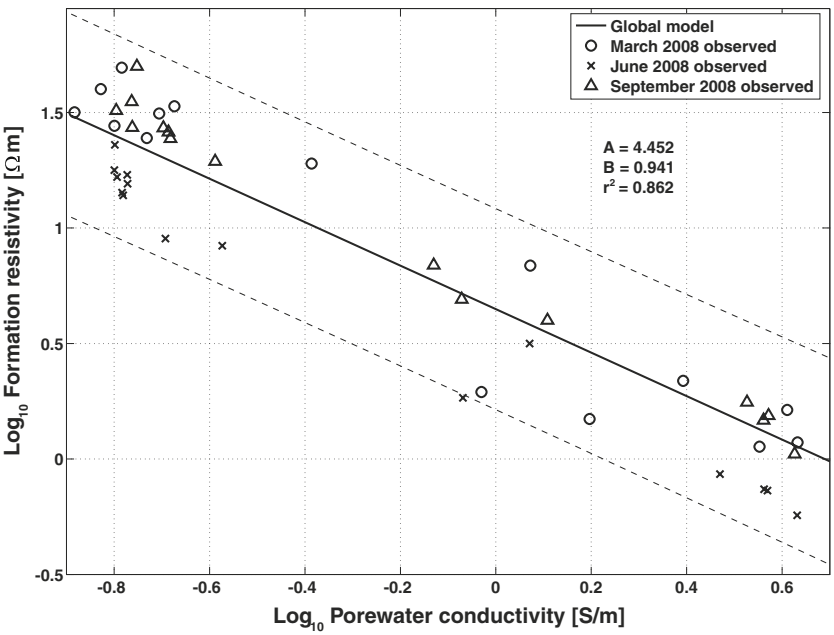

Fig. 7 Observed electrical conductivity of porewater and estimates of formation resistivity. 95% prediction limits (*dashed line*) and Eq. 7 model parameters A and B and correlation coefficient r^2

 DOI 10.1007/s10040-009-0503-6

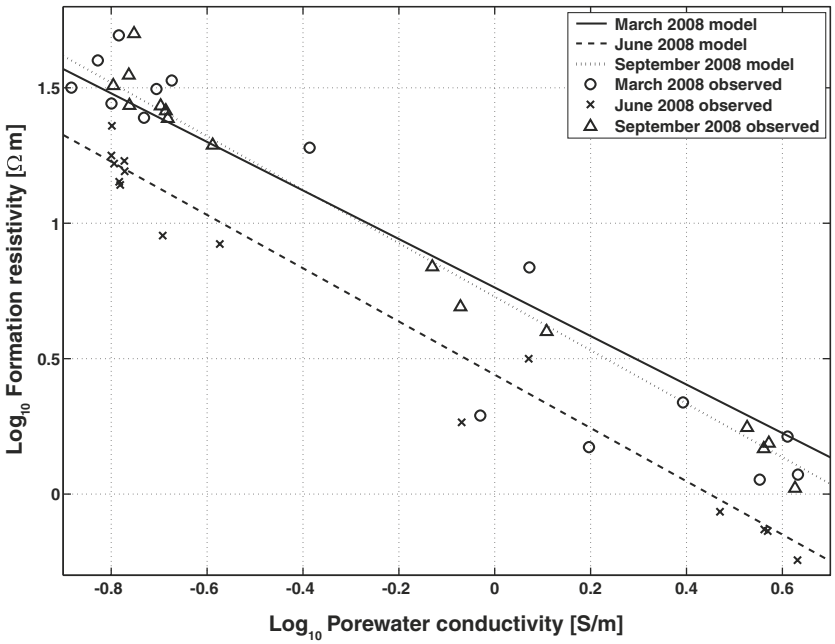

Fig. 8 Observed electrical conductivity of porewater and estimates of formation resistivity. Models are based on observations from March, June and September separately

winds raising the average sea level, hydraulic heads were increased by 15–20 cm in the period from June–September. The sea level increased from −3 cm to a tidal peak at 18 cm ultimately decreasing to −1 cm during the profiling. The coastline was ~65 m from E5. In September, a freshwater zone of 0.10–0.24 S/m reaches −2.1 m at E1, −2.5 m at E2, and −3.1 m at E3 and E4, topping a brackish zone where porewater conductivity gradually increases from 0.24 to 4.00 Ωm. The width of the transition zone between freshwater and brackish water varies from 0.75 m at E1, 1 m at E2 and E3, to 1.25 m at E4. At E5, porewater conductivities increase from 0.50 to 1.00 S/m between −1.2 and 0.8 m to ~1.00–1.50 S/m below −1.2 m.

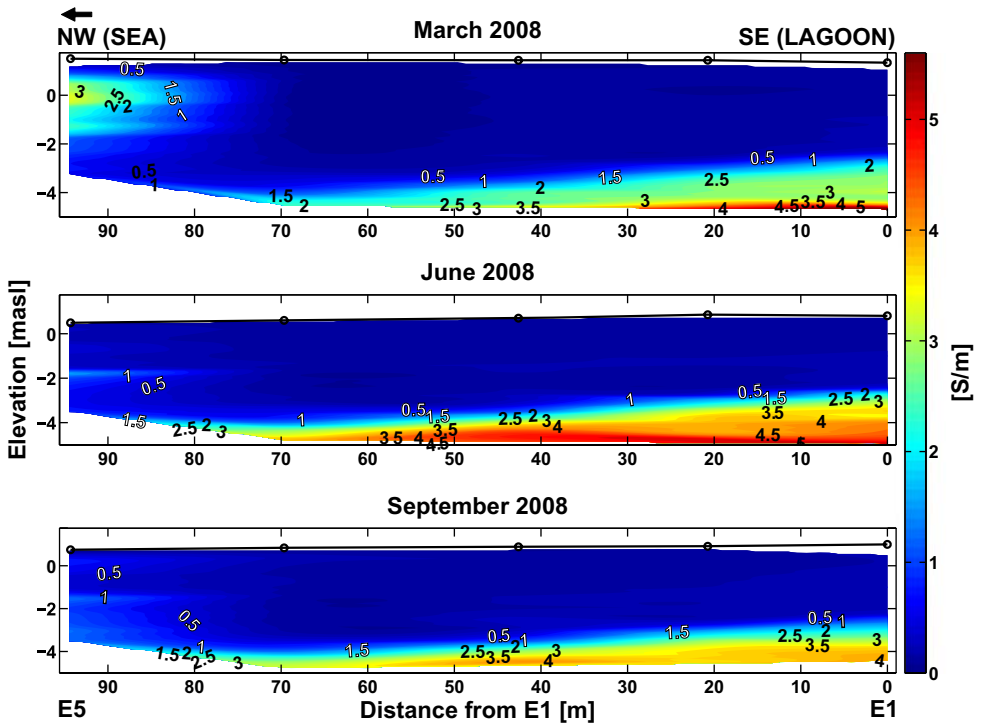

Fig. 9 Electrical conductivity of porewater in March, June and September 2008 based on VMEP, equidistance=0.05 S/m, water table (*thick horizontal line*) and probe position (*circle*)

 DOI 10.1007/s10040-009-0503-6

Conclusions

Vertical, geoelectrical, multielectrode probes, each accompanied by three piezometers screened at different depths, have been installed at five positions along a bay barrier profile on the west coast of Denmark. Resistivity data were collected by measuring gradient and dipole-dipole configurations. The profiles were processed and poor data discarded by visually inspecting apparent resistivity values plotted against their vertical position, eliminating 0.8% of the data with no systematic pattern in outliers. An interpretation of the processed resistivity data was performed by regularized inversion using a one-dimensional, horizontally layered model of formation resistivity with a vertical resolution of 0.25 m. The standard deviation of estimated model layer resistivity was between 0.01–0.03 while data residuals spanned 1.0–4.1, largest for E1 and E5 in March and September.

Porewater conductivity was related to formation resistivity by a power function in which two parameters were estimated using observed porewater conductivity and corresponding estimated formation resistivity gathered in March, June, and September 2008. The general conversion between estimated formation resistivity and porewater conductivity applies well to the March and September profiles while the observations gathered in June differ significantly from the model for September. The cause of this disagreement is unresolved. Further studies of the relationship between formation resistivity and porewater conductivity are necessary to investigate this discrepancy.

By interpreting the geoelectrical profiling data together with water-table measurements, detailed information about the extent of the freshwater lens, the position and width of the transition between fresh and brackish water, were obtained along the VMEP profile in March, June, and September 2008.

Results show that a high average sea level combined with favorable recharge conditions through January–February raised the hydraulic head to 1.3–1.5 m and increased the thickness of the freshwater lens in March to 5 m. In March and June, a hydraulic gradient towards the lagoon was observed between E1 and E2. This may be attributed to aquifer discharge into lagoon surface water which provides a pathway for rapid surface-water runoff towards the canal in the lagoon (Fig. 1). As a result, the freshwater body appears lens-shaped in this situation, as water discharges landward and seaward on each side of a water-divide situated in the dune. In March, saline water topped freshwater at E5, which may be attributed to wave run-up and spindrift. The transition zone from fresh to brackish water increased in thickness from 0.75 m at E1–E2 and 1 m at E3 to 1.25 m at E4.

The period prior to June was characterized by low precipitation and increasing evapotranspiration ultimately ceasing the recharge of the aquifer, and resulting in a decrease of 0.5–0.86 m in hydraulic head and a reduction in the thickness of the freshwater lens by 80 cm. In June, the transition zone between freshwater and salt water extended 0.5 m at E1–E2, 0.75 m at E3 and 1 m at E4.

During the autumn of 2008, the precipitation increased significantly which combined with a seasonal decrease in evapotranspiration increased the recharge prior to September. The average sea level increased with prevailing onshore winds, promoting wave run-up and spindrift resulting in more saline conditions in the upper part of the aquifer at E5. Hydraulic heads increased to 0.75–1.0 m, the thickness of the freshwater lens was increased by 30 cm and the transition from fresh to brackish water occurred over 0.75 m at E1, 1 m at E2 and E3 to 1.25 m at E4. At E5 the transition zone is not readily defined.

Although a displacement of the freshwater/salt-water interface is to be expected under dry conditions, the position of the freshwater/salt-water interface was situated at approximately the same depth in March, June, and September. As the average sea level is low in April–May, two opposing forces act on the freshwater lens. The reduced thickness of the freshwater zone will move the freshwater/salt-water interface upwards while a lower sea level will increase discharge from the aquifer but also move the interface downwards. The low hydraulic conductivity, silty sand from −1 to −9 m may limit the exchange of water from the upper, highly conductive, sandy sediment, promoting more stationary conditions in the deeper parts of the aquifer.

Acknowledgements Cheminova, Region Midtjylland and the Aarhus University Research Foundation are thanked for funding this study. We most kindly thank the reviewers Dr. Todd Halihan and Dr. Rory Henderson whose suggestions and comments improved the paper significantly. We also wish to thank The Danish Coastal Authority (Kystdirektoratet) for providing sea level observations.

References

Archie G (1942) The electrical resistivity log as an aid in determining some reservoir characteristics. Trans AIME Eng 146:54–61

Bouzouf B, Ouazar D, Himi M, Casas A, Elmahi I, Benkhaldoun F (2001) Integrating hydrogeochemical and geophysical data for testing a finite volume based numerical model for saltwater intrusion. Transp Porous Media 43:179–194

Bringas JE (2004) Handbook of comparative world steel standards, 3rd edn. ASTM International, West Conshohocken, PA, USA

Burnett WC, Peterson R, Moore WS, de Oliveira J (2008) Radon and radium isotopes as tracers of submarine groundwater discharge: results from the Ubatuba Brazil SGD assessment intercomparison. Estuar Coast Shelf Sci 76:501–511

Cartwright N, Nielsen P, Dunn S (2003) Water table waves in an unconfined aquifer: experiments and modeling. Water Resour Res 39(12), 1330. doi:10.1029/2003WR002185

Charette MA, Splivallo R, Herbold C, Bollinger MS, Moore WS (2003) Salt marsh submarine groundwater discharge as traced by radium isotopes. Mar Chem 84:113–121

Choudhury K, Saha DK, Chakraborty P (2001) Geophysical study for saline water intrusion in a coastal alluvial terrain. J Appl Geophys 46:189–200

Christensen FD, Engesgaard P (2000) Reactive transport modelling of saltwater intrusion in a shallow aquifer. In: Bjerg PL, Engesgaard P, Krom TD (eds) Groundwater 2000. Balkema, Rotterdam, the Netherlands

Christensen NB (1990) Optimized fast Hankel transform filters. Geophys Prospect 38(5):545–568

Christensen S (1994) Hydrological model for the Tude Å catchment. Nord Hydrol 25:145–166

Dahlin T, Zhou B (2004) A numerical comparison of 2D resistivity imaging with 10 electrode arrays. Geophys Prospect 52(5):379–398 ISSN 0016-8025

Daniels JJ (1978) Interpretation of buried electrode resistivity data using a layered earth model. Geophysics 43(5):988–1001

Draper NR, Smith H (1981) Applied regression analysis, 2 edn. Wiley, New York

Duque C, Calvache ML, Pedrera A, Martin-Rosales W, Lopez-Chicano M (2008) Combined time domain electromagnetic soundings and gravimetry to determine marine intrusion in a detrital coastal aquifer (southern Spain). J Hydrol 349:536–547

Inman JR, Ryu J, Ward SH (1973) Resistivity inversion. Geophysics 38(6):1088–1108

Kafri U, Goldman M, Lang B (1997) Detection of subsurface brines, freshwater bodies and the interface configuration in-between by the time domain electromagnetic method in the Dead Sea rift, Israel. Environ Geol 31:42–49

Koukadaki MA, Karatzas GP, Papadopoulou MP, Vafidis A (2007) Identification of the saline zone in a coastal aquifer using electrical tomography data and simulation. Water Resour Manage 21:1881–1898

Kovac G (1981) Seepage hydraulics. Elsevier, Amsterdam

Li L, Barry DA, Pattiaratchi CB (1997) Numerical modelling of tide-induced beach water table fluctuations. Coast Eng 30:105–123

Li L, Barry DA, Stagnitti F, Parlange JY (1999a) Groundwater waves in a coastal aquifer: a new governing equation including vertical effects and capillarity. Water Resour Res 35:3253–3259

Li L, Barry DA, Stagnitti F, Parlange JY (1999b) Submarine Groundwater Discharge and associated chemical input to a coastal sea. Water Resour Res 35:3253–3259

Mao X, Barry DA, Li L, Binley A, Jeng DS (2005) Tidal influence on behavior of a coastal aquifer adjacent to a low-relief estuary. J Hydrol 327:110–127

Menke W (1989) Geophysical data analysis: discrete inverse theory. Academic, San Diego

Michael HA, Mulligan AE, Harvey CF (2005) Seasonal oscillations in water exchange between aquifers and the coastal ocean. Nature 431:1145–1148

Moore WS (2007) Estimating submarine groundwater discharge in the range 10^{1} to 10^{8} km^{2} using Ra isotopes. Geochim Cosmochim Acta 71:A684–A684

Moore WS, de Oliveira J (2008) Determination of residence time and mixing processes of the Ubatuba, Brazil, inner shelf waters using natural Ra isotopes. Estuar Coast Shelf Sci 76:512–521

Nielsen P (1990) Tidal dynamics of the water table in beaches. Water Resour Res 26:2127–2134

Nielsen P, Aseervatham AM, Fenton JD, Perrochet P (1997) Groundwater waves in aquifers of intermediate depths. Adv Water Resour 20:37–43

Oberdorfer JA (2003) Hydrogeologic modeling of submarine groundwater discharge: comparison to other quantitative methods. Biogeochemistry 66:159–169

Povinec PP, Aggarwal PK, Aureli A, Burnett WC, Kontar EA, Kulkarni KM, Moore WS, Rajar R, Taniguchi M, Comanducci JF, Cusimano G, Dulaiova H, Gatto L, Groening M, Hauser S, Levy-Palomo I, Oregioni B, Ozorovich YR, Privitera AMG, Schiavo MA (2006) Characterisation of submarine groundwater discharge offshore south-eastern Sicily. J Environ Radioact 89:81–101

Serban DZ, Jacobsen BH (2001) The use of broad-band prior covariance for inverse palaeoclimate estimation. Geophys J Int 147(1):29–40

Shtivelman V, Goldman M (2000) Integration of shallow reflection seismics and time domain electromagnetics for detailed study of the coastal aquifer in the Nitzanim area of Israel. J Appl Geophys 44:197–215

Smith L, Zawadzki W (2003) A hydrogeologic model of submarine groundwater discharge: Florida intercomparison experiment. Biogeochemistry 66:95–110

Swarzenski WP, Simonds WF, Paulson AJ, Kruse S, Reich C (2007) Geochemical and geophysical examination of submarine groundwater discharge and associated nutrient loading estimates into Lynch Cove, Hood Canal, WA. Environ Sci Technol 41:7022–7029

Tarantola A (1987) Inverse problem theory. Elsevier, Amsterdam

Turner IL (1993) Water table outcropping on macro-tidal beaches: a simulation model. Mar Geol 115:227–238

Turner IL, Ackworth RI (2004) Field measurements of beachface salinity structure using cross-borehole resistivity imaging. J Coast Res 20:753–760

Turner IL, Coates BP, Acworth IR (1996) The effect of tides and waves on water-table elevations in coastal zones. Hydrogeol J 4:51–69

Vandenbohede A, Lebbe L (2006) Occurrence of salt water above fresh water in dynamic equilibrium in a coastal groundwater flow system near De Panne, Belgium. Hydrogeol J 14:462–472

Vouillamoz JM, Chatenoux B, Mathieu F, Baltassat JM, Legchenko A (2007) Efficiency of joint use of MRS and VES to characterize coastal aquifer in Myanmar. J Appl Geophys 61:142–154

Woolf D, Challenor P, Cotton P (2002) Variability and predictability of the North Atlantic wave climate. J Geophys Res 107(C10), 3145. doi:10.1029/2001JC001124

Young MB, Gonneea ME, Fong DA, Moore WS, Herrera-Silveira J, Paytan A (2008) Characterizing sources of groundwater to a tropical coastal lagoon in a karstic area using Radium isotopes and water chemistry. Mar Chem 109:377–394